Article

Evolution of Free Volumes in Polycrystalline BaGa$_2$O$_4$ Ceramics Doped with Eu^{3+} Ions

Halyna Klym [1,*], **Ivan Karbovnyk** [1,2], **Andriy Luchechko** [1,2], **Yuriy Kostiv** [1], **Viktorija Pankratova** [3] **and Anatoli I. Popov** [3,*]

[1] Specialized Computer Systems Department, Lviv Polytechnic National University, 12 Bandera Str., 79013 Lviv, Ukraine; ivan.karbovnyk@lnu.edu.ua (I.K.); andriy.luchechko@lnu.edu.ua (A.L.); yura.kostiv@gmail.com (Y.K.)

[2] Department of Electronics and Computer Technologies, Ivan Franko National University of Lviv, 50 Dragomanov Str., 79005 Lviv, Ukraine

[3] Institute of Solid State Physics, University of Latvia, Kengaraga 8, LV-1063 Riga, Latvia; viktorija.pankratova@cfi.lu.lv

[*] Correspondence: halyna.i.klym@lpnu.ua (H.K.); popov@latnet.lv (A.I.P.)

Abstract: BaGa$_2$O$_4$ ceramics doped with Eu^{3+} ions (1, 3 and 4 mol.%) were obtained by solid-phase sintering. The phase composition and microstructural features of ceramics were investigated using X-ray diffraction and scanning electron microscopy in comparison with energy-dispersive methods. Here, it is shown that undoped and Eu^{3+}-doped BaGa$_2$O$_4$ ceramics are characterized by a developed structure of grains, grain boundaries and pores. Additional phases are mainly localized near grain boundaries creating additional defects. The evolution of defect-related extended free volumes in BaGa$_2$O$_4$ ceramics due to the increase in the content of Eu^{3+} ions was studied using the positron annihilation lifetime spectroscopy technique. It is established that the increase in the number of Eu^{3+} ions in the basic BaGa$_2$O$_4$ matrix leads to the agglomeration of free-volume defects with their subsequent fragmentation. The presence of Eu^{3+} ions results in the expansion of nanosized pores and an increase in their number with their future fragmentation.

Keywords: ceramics; doping; free-volume defects; positron annihilation; agglomeration; fragmentation

1. Introduction

BaGa$_2$O$_4$ ceramics are considered to be promising material for use as an insulator in optoelectronic devices [1,2], as a secondary coating for plasma panels [3–5], etc. [6]. The doping of impurities in the form of rare-earth ions leads to the expansion of the functional properties of such ceramics [7]. Spinel compounds doped with transition metal ions are promising due to the number of ways to tailor the luminescence spectrum by adjusting the impurity content or by influencing the localization of the dopant in the structure.

The investigation of materials similar to BaGa$_2$O$_4$ ceramics in both undoped and doped forms is mainly focused on the study of their luminescent properties [1,8–14]. Ceramics are a double oxide belonging to the quadrilateral frame topologies that exist in multiple polymorphs, which is important for luminescence studies because it exhibits luminescence without the inclusion of rare-earth ions. However, the most interesting are rare-earth-doped BaGa$_2$O$_4$ ceramics. Most investigations of such material are limited to X-ray diffraction (XRD), optical studies, etc. [15–19]. Nevertheless, the doping of such ceramics not only leads to the modification of their luminescent properties and changes in phase composition, but also causes structural transformation [20,21]. This significantly transforms the inner structure of ceramics forming additional defect-related free volumes [22–27].

One promising method (as an alternative and addition to traditional ones) for studying the free volume in solids of different structural types is positron annihilation lifetime

(PAL) spectroscopy [28,29]. This technique has long been considered for the structural analysis of functional materials such as ceramics [30–32], glass [33,34], polymers [35,36], nanocomposites [37,38], etc. Scientific groups that are actively working in this direction have presented different approaches to the analysis of the PAL spectra of ceramic materials and their decomposition into different numbers of components [39–41]. We have also conducted a lot of research using the PAL method to study changes in free volume in spinel ceramics [42], chalcogenide glasses [43] under the influence of technological modification, etc. It was shown that functional ceramics are characterized by the decomposition of the PAL spectrum into two, three and four components depending on the developed porous structure of materials. Knowledge about the mechanisms of inner free-volume transformations is crucial for facilitating advances in the design and control of ceramics microstructure. This is required to optimize properties that enable efficient scintillation features in various applications.

It was shown that for functional ceramic materials two PAL channels are possible: the capturing of positrons by bulk defects with short and medium positron lifetimes, as well as the channel of decay of ortho-positronium (o-Ps) atoms with a long lifetime. The short-term component reflects the microstructural features of the main phase, the middle one is connected with defect-related voids near grain boundaries and the lifetime of the long-term component can estimate the transformation of nanopores. However, the study of $BaGa_2O_4$ ceramics using the PAL method has not yet been conducted. Therefore, the goal of this work was to study the transformations of inner free volumes (extended defects at grain boundaries and nanopores) in $BaGa_2O_4$ ceramics doped with different amounts of Eu^{3+} ions using the PAL method in combination with XRD and scanning electron microscopy (SEM) techniques.

2. Materials and Methods

Samples of pure $BaGa_2O_4$ ceramics and those with Eu^{3+} impurities were prepared using high-temperature solid-phase synthesis. Powders of $BaCO_3$ and Ga_2O_3 oxides with purities of 99.99% were taken as starting components for synthesis. Isopropyl CH_3-$CH(OH)$-CH_3 alcohol was also used in the sintering of $BaGa_2O_4$-based ceramics [44].

The oxide mixtures were taken at a stoichiometric ratio of 1:1 mol per 2 g of raw material. The content of the Eu^{3+} ions (Eu_2O_3 with a purity of 99.99%) was determined to replace the equivalent molar content of Ga and Ba. The amount of Eu^{3+} ions was 0, 1, 3 and 4 mol.%. The oxide mixture was stirred thoroughly in an agate solution for 6 h with the addition of isopropyl alcohol. The obtained raw material was air-dried for 1 h at a temperature of 80 °C. After that, the raw material was pressed under a pressure of 150 kg/cm^2, obtaining workpieces with a diameter of 6 mm and a thickness of 1.5 mm. The blanks were placed on a platinum substrate and annealed in a furnace at 1200 °C for 12 h in air. In the next stage, annealing was performed at 1300 °C for 5 h. The final ceramic samples were in the form of tablets with a diameter of 4 mm and a thickness of 1 mm.

X-ray examinations were performed using a STOE STADI P (STOE & Cie GmbH, Darmstadt, Germany) diffractometer. The source of the X-rays was a copper anode tube with Cu Kα1 radiation (λ = 1.5406 Å). The investigated range of diffraction angles used was from 2 to 100° with a minimum measurement step of 0.005°. The microstructural study of grains, grain boundaries and pores in the $BaGa_2O_4$ ceramics doped with Eu^{3+} ions was investigated using a high-resolution ZEISS Ultra Plus SEM (Carl Zeiss Microscopy Deutschland GmbH, Zeiss, Germany) with two secondary electron detection systems including elementary compositions analysis.

The ORTEC system with a ^{22}Na isotope as a positron source was used for PAL measurements. Investigations were performed at 22 °C and a relative humidity of 35% for two identical ceramic samples placed in a sandwich configuration as described in [45].

The measured PAL spectra were calculated using LT software [46] in a three-component fitting procedure (lifetimes τ_1, τ_2, τ_3 and intensities I_1, I_2, I_3) for spinel ceramics with a branched porous structure [45]. Parameters, such as the average lifetime of positrons τ_{av},

the lifetime of positrons in defect-free bulk τ_b and the rate of positron trapping in defects κ_d, were obtained using a two-stage positron trapping model [45]. We also determined the $\tau_2 - \tau_b$ difference (which describes the size of the free-volume defects where positrons are trapped) and the τ_2/τ_b ratio (which correlates with the nature of defects). Using the lifetime of the third component, the radii of the nanopores (R_3) were determined using the Tao–Eldrup model [47].

3. Results and Discussion

According to the results of the XRD investigations [44], the initial undoped $BaGa_2O_4$ ceramics contain three phases: 34.2 wt.% of the main $BaGa_2O_4$ phase, 58.5 wt.% of the additional $Ba_{2.84}Ga_{11.32}O_{19.82}$ phase and 7.3 wt.% of the Ga_2O_3 phases. The $BaGa_2O_4$ ceramics with 1 mol.% Eu^{3+} ions are single-phase. The $BaGa_2O_4$ ceramics with a 3 and 4 mol.% impurity of Eu^{3+} ions contain two phases: 97.3 and 96.7 wt.% of the $BaGa_2O_4$ phase as well as 2.7 and 3.3 wt.% of the additional Eu_3GaO_6 phase, respectively. The results of the detailed XRD analysis using Rietveld's method are represented in Table 1.

Table 1. Phase composition and Rietveld refined parameters for undoped and Eu^{3+}-doped $BaGa_2O_4$ ceramics.

Sample	Number of Phases	Phases, Lattice Parameters, Weight Fraction
$BaGa_2O_4$	3 phases: $BaGa_2O_4$, $Ba_{2.84}Ga_{11.32}O_{19.82}$ and Ga_2O_3	$BaGa_2O_4$: a = 18.619(1) Å, c = 8.670(1) Å fraction 34.2 wt.% $Ba_{2.84}Ga_{11.32}O_{19.82}$: a = 15.807(1) Å, b = 11.687(1) Å, c = 5.136(1) Å, β = 107.62(1) Å, fraction 58.5 wt.% Ga_2O_3: a = 12.213(4) Å, b = 3.042(1) Å, c = 5.810(2) Å, β = 103.65(3) Å, fraction 7.3 wt.%
$BaGa_2O_4$ + 1 mol.% Eu^{3+}	1 phase: $(Ba,Eu)Ga_2O_4$	$(Ba,Eu)Ga_2O_4$: a = 18.605(1) Å, c = 8.670(1) Å, fraction 100 wt.%
$BaGa_2O_4$ + 3 mol.% Eu^{3+}	2 phases: $BaGa_2O_4$, Eu_3GaO_6	$BaGa_2O_4$: a = 18.620(1) Å, c = 8.658 (1) Å, fraction 97.3 wt.% Eu_3GaO_6: a = 9.026 (2) Å, b = 11.344(2) Å, c = 5.496(1) Å, fraction 2.7 wt.%
$BaGa_2O_4$ + 4 mol.% Eu^{3+}	2 phases: $BaGa_2O_4$, Eu_3GaO_6	$BaGa_2O_4$: a = 18.622(1) Å, c = 8.658(1) Å, fraction 96.7 wt.% Eu_3GaO_6: a = 9.031(2) Å, b = 11.343(2) Å, c = 5.497(1) Å, fraction 3.3 wt.%

Generalized XRD patterns for undoped $BaGa_2O_4$ ceramics and those doped with Eu^{3+} ions, in comparison with the diffraction pattern of $BaGa_2O_4$ in the ICSD reference data file, are shown in Figure 1. The availability of the main phase in the studied ceramics indicates peaks at the reflection angle 2θ of 28.12°.
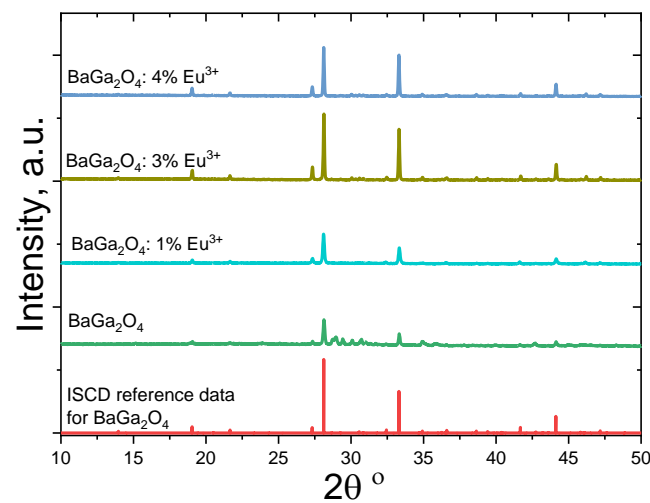
Figure 1. XRD patterns for undoped and Eu^{3+}-doped $BaGa_2O_4$ ceramics in comparison with ICSD reference data for $BaGa_2O_4$.

As can be seen from the SEM images, both undoped $BaGa_2O_4$ ceramics (Figure 2a) as well as ceramics with 1 mol.% Eu^{3+} ions (Figure 2b) have a fairly branched structure of grains, grain boundaries and pores of different forms and shapes [45]. Samples of these ceramics are characterized by a small grain size and homogeneity in the morphology of the structure. The presence of Eu^{3+} ions leads to an increase in the pore size of the initial $BaGa_2O_4$ ceramics, the formation of grain agglomerates and their further growth. In addition, in both cases there is the formation of micro- and nanosized crystals on the grain surface.
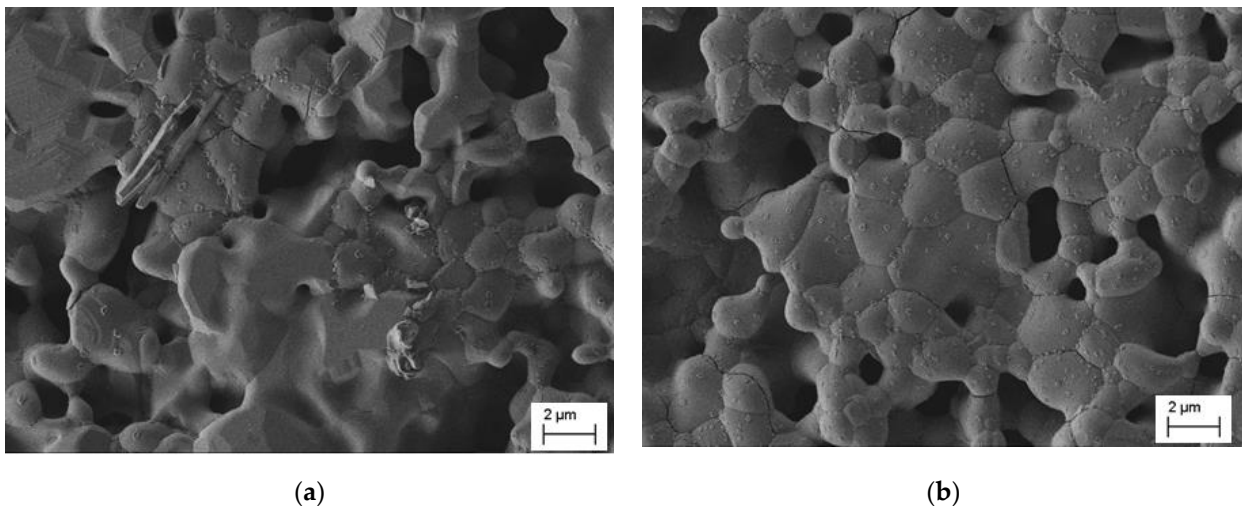

(**a**)   (**b**)

Figure 2. SEM images for undoped (**a**) and Eu^{3+}-doped (**b**) $BaGa_2O_4$ ceramics.

In addition, the elemental composition of the studied ceramic samples was evaluated using the method of energy-dispersion X-ray (EDX) spectroscopy for selected areas (Figure 3).

It is known that the accuracy of the EDX technique depends on the nature of the sample and other factors so only clearly defined peaks were analyzed. As can be seen from Figure 3a, elements in the $BaGa_2O_4$ compound are evenly distributed over the volume of crystallites, and there are reflexes of the main elements of the material. However, in the sample of $BaGa_2O_4$ ceramics doped with 1 mol.% Eu^{3+} ions (Figure 3b), their percentage was not established (despite the presence of Eu-reflexes). Obviously, such a small number of Eu^{3+} ions is not enough to identify the selected area. For $BaGa_2O_4$ ceramics with 3 mol.% Eu^{3+} ions, the presence of the latter increases to 0.74% (Figure 3c), while a further rise in the

content of impurities (to 4 mol.% Eu^{3+} ions) leads to a significant increase in the material to 4.88% (Figure 3d, Table 2). Thus, the obtained results indicate the successful incorporation of Eu^{3+} ions into the $BaGa_2O_4$ matrix, especially if their concentration exceeds 1 mol.%.
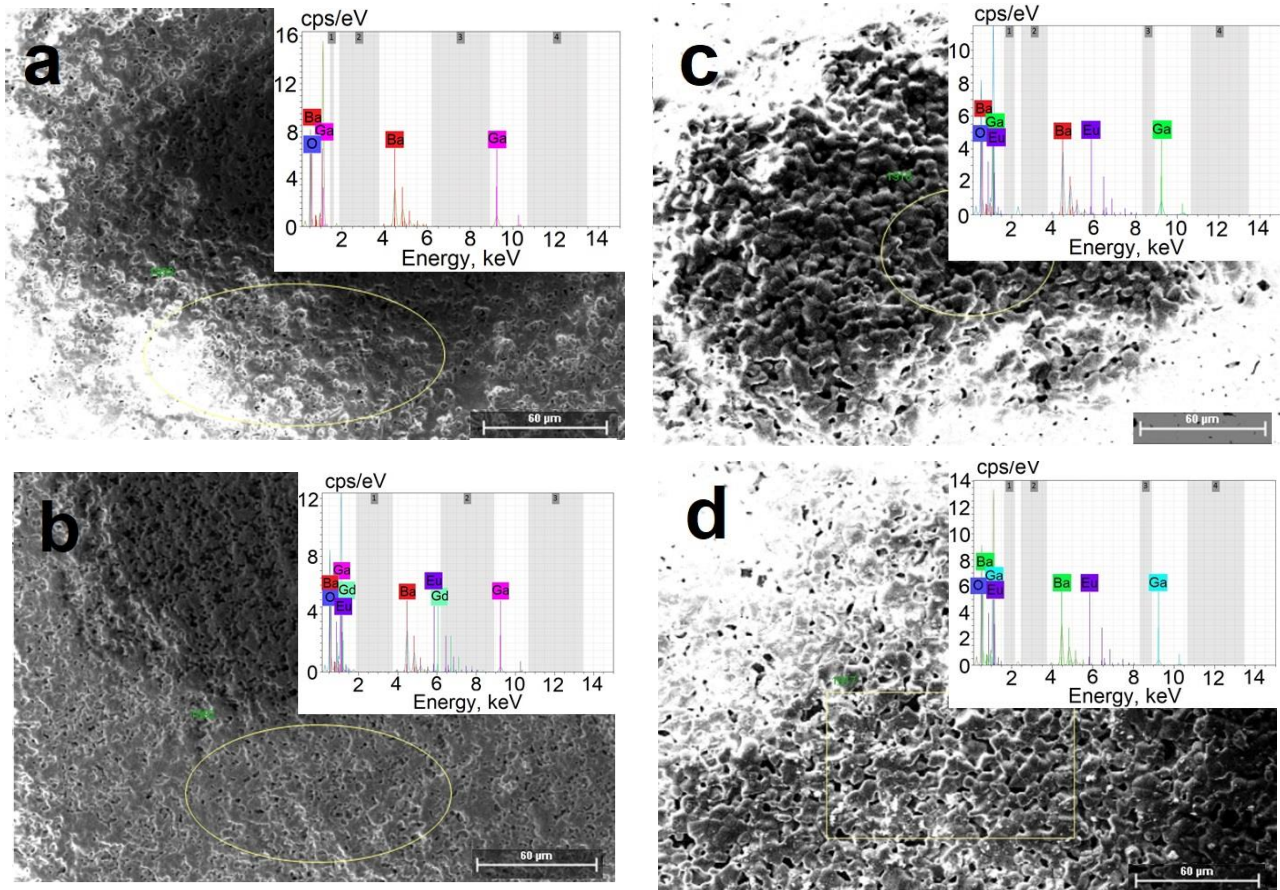

Figure 3. Microstructure of the selected areas and elemental composition of the undoped $BaGa_2O_4$ ceramics (**a**) and those doped with 1 mol.% (**b**), 3 mol.% (**c**) and 4 mol.% of Eu^{3+} ions (**d**).

Table 2. Elemental composition of the undoped and Eu^{3+}-doped $BaGa_2O_4$ ceramics.

Sample	Mass, %				Atom, %			
	O	Ga	Ba	Eu	O	Ga	Ba	Eu
$BaGa_2O_4$	16	34	30	-	59	28	13	-
$BaGa_2O_4$ + 1 mol.% Eu^{3+}	17	16	29	-	71	15	14	-
$BaGa_2O_4$ + 3 mol.% Eu^{3+}	16	30	44	0.74	59	25	15	0.28
$BaGa_2O_4$ + 4 mol.% Eu^{3+}	16	25	32	4.88	61	22	15	1.98

Obviously, the presence of different amounts of Eu^{3+} ions in the ceramic $BaGa_2O_4$ matrix will modify their inner free volume. Extended defects formed in ceramic materials and mainly localized near grain boundaries are also due to the release of additional phases. The PAL method was used to study such defect-related free volumes in undoped and Eu^{3+}-doped $BaGa_2O_4$ ceramics.

The fitting parameters of PAL spectra for the studied ceramics calculated within a three-component procedure are presented in Table 3. It is established that with rising Eu^{3+} content in the $BaGa_2O_4$ matrix, an increase in the lifetime τ_1 and intensity I_1 of the first short-term component is observed. Most probably, the structure of the mail phase of the ceramics is improved. However, when the Eu^{3+} ions increase to 4 mol.%, the opposite trend occurs. The lifetime τ_2 of the second component increases and intensity I_2 decreases

with Eu^{3+} content (to 3 mol.%), while a further rise in Eu^{3+} ions (to 4 mol.%) leads to a decreased τ_2 and an increased I_2.

Table 3. Lifetimes and intensities for undoped and Eu^{3+}-doped $BaGa_2O_4$ ceramics obtained in three-component fitting procedure.

Sample	τ_1 (±0.002), ns	I_1 (±0.1), %	τ_2 (±0.001), ns	I_2 (±0.1), %	τ_3 (±0.001), ns	I_3 (±0.1), %
$BaGa_2O_4$	0.200	83.3	0.424	14.9	2.196	1.8
$BaGa_2O_4$ + 1 mol.% Eu^{3+}	0.206	85.0	0.450	13.2	2.289	1.8
$BaGa_2O_4$ + 3 mol.% Eu^{3+}	0.212	89.9	0.550	7.9	2.390	2.2
$BaGa_2O_4$ + 4 mol.% Eu^{3+}	0.201	83.3	0.411	14.4	2.157	2.4

As noted in [42,45], the lifetime τ_2 of the second component should be associated with the capture of positrons by defect-related free volumes. According to XRD data, undoped $BaGa_2O_4$ ceramics contain a large number of additional phases. As shown by the SEM method, these phases are unevenly distributed in the volume of the ceramic and are mainly localized near the grain boundaries. The extracted phases play the role of special centers of positron capture in the volume of ceramics. Since undoped $BaGa_2O_4$ ceramics contain two additional phases, positrons in such samples will be better captured.

The lifetime τ_2 correlates with the size of the free-volume defects, where positrons are captured, and the intensity correlates with their number. Thus, when the Eu^{3+} content increases to 3 mol.%, the agglomeration of free-volume defects occurs, while the supersaturation of the $BaGa_2O_4$ matrix with Eu^{3+} (up to 4 mol.%) leads to their fragmentation. The identified trends (Table 4) correlate with the positron trapping parameters calculated within the two-state positron trapping model [45]. Schematically, the evolution of defect-related free volumes near grain boundaries with increasing Eu^{3+} ions in $BaGa_2O_4$ ceramics is shown in Figure 4.

Table 4. Positron trapping parameters and nanopore radius for undoped and Eu^{3+}-doped $BaGa_2O_4$ ceramics.

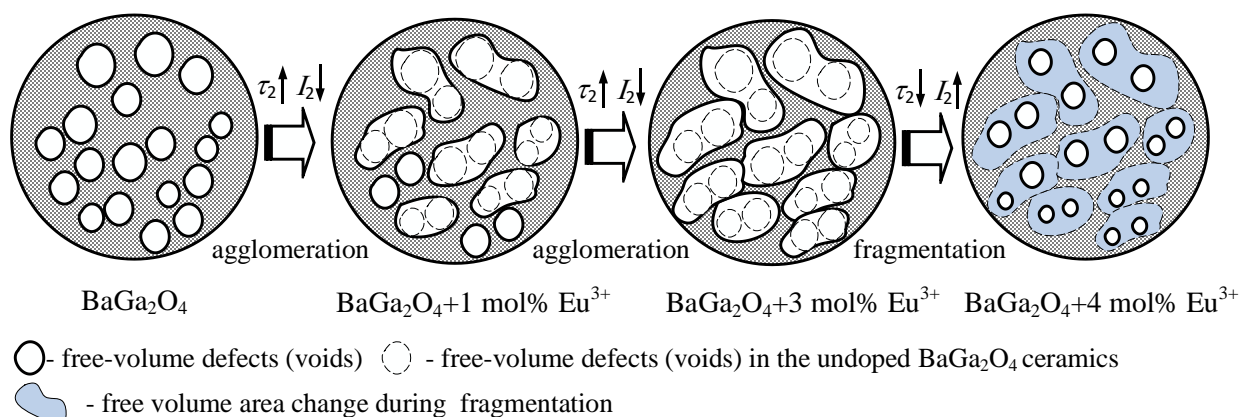| Sample	τ_{av}, ns	τ_b, ns	κ_d, ns^{-1}	$\tau_2 - \tau_b$, ns	τ_2/τ_b	R_3, nm
$BaGa_2O_4$	0.234	0.218	0.40	0.21	1.95	0.306
$BaGa_2O_4$ + 1 mol.% Eu^{3+}	0.239	0.222	0.35	0.23	2.02	0.314
$BaGa_2O_4$ + 3 mol.% Eu^{3+}	0.240	0.223	0.23	0.33	2.46	0.322
$BaGa_2O_4$ + 4 mol.% Eu^{3+}	0.232	0.218	0.37	0.19	1.89	0.302

Figure 4. Diagram explaining the evolution of defect-related voids in $BaGa_2O_4$ ceramics caused by Eu^{3+} doping.

As mentioned above, the lifetime of the second component correlates with the size of the free-volume defect, while its intensity is defined by the amount of these defects. The agglomeration process is reflected in the increase in the second component's lifetime and in the decrease in its intensity. Solid lines in Figure 4 show existing voids in the sample,

and dotted lines indicate voids in the initial ceramics. This schematically illustrates the process when two smaller voids are joined to form a larger one.

As can be seen from Table 3, lifetime τ_2 increases from 0.424 ns in $BaGa_2O_4$ ceramics to 0.450 ns in $BaGa_2O_4$ ceramics containing 1 mol.% Eu^{3+} ions, and intensity decreases from 14.9 to 13.2%.In Figure 4, it is schematically demonstrated that most voids were agglomerated, though there were some left unchanged. Generally, the number of voids is smaller and the overall volume of the voids is larger. For $BaGa_2O_4$ ceramics doped with 3 mol.% Eu^{3+} ions, agglomeration is also the case, and the lifetime of the second component keeps increasing up until 0.550 ns, whereas intensity goes down to 7.9%. It is schematically shown that the voids in $BaGa_2O_4$ ceramics with 1 mol.% Eu^{3+} ions were unchanged; in $BaGa_2O_4$ ceramics with 3 mol.% Eu^{3+} ions, they were involved in agglomeration. That is why the number of voids decreased even more and the overall void volume became larger. For $BaGa_2O_4$ ceramics with 4 mol.% Eu^{3+} we observe the opposite—fragmentation of free-volume defects occurs. These changes are manifested in the decrease in τ_2 lifetime and the increase in I_2 intensity. In Figure 4, the region where free-volume voids change compared to $BaGa_2O_4$ ceramics with 3 mol.% Eu^{3+} ions due to fragmentation is shown in blue. The intensity I_2 for $BaGa_2O_4$ ceramics with 4 mol.% Eu^{3+} ions is close to the I_2 for undoped $BaGa_2O_4$ ceramics, but the lifetime τ_2 is shorter. This is evidence of the smaller overall size of free-volume defects in $BaGa_2O_4$ ceramics with 4 mol.% Eu^{3+} ions.

The third long-term component of the PAL spectrum (the second channel of positron annihilation with lifetime τ_3 and intensity I_3) is associated with the o-Ps decaying in nanopores [45]. As can be seen from Table 3, lifetime τ_3 and intensity I_3 increase with Eu^{3+} content in the $BaGa_2O_4$ ceramics (to 3 mol.%). However, when the amount of Eu^{3+} ions rises to 4 mol.%, the lifetime τ_3 decreases and the intensity I_3 continues to increase. It is obvious that the presence of Eu^{3+} ions in the ceramic matrix leads to the expansion of nanosized pores and an increase in their number. However, the supersaturation of ceramics with doped ions (to 4 mol.%) results in the fragmentation of nanopores. The obtained trends are reflected in the radius of nanopores R_3 (Table 4) calculated using the Tao–Eldrup model. This process is schematically shown in Figure 5.
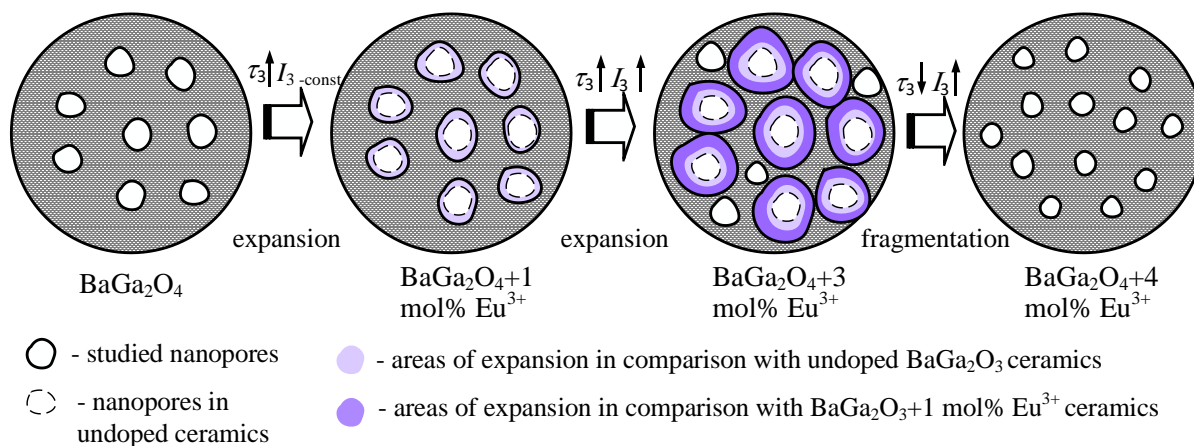

Figure 5. Diagram explaining the evolution of nanopores in $BaGa_2O_4$ ceramics caused by Eu^{3+} doping.

Adding 1 mol.% Eu^{3+} to the $BaGa_2O_4$ ceramics is reflected in the increased lifetime of the third component (up to 2.289 ns) at a constant intensity I_3 as compared to the undoped ceramics. This confirms the process of nanopore volume expansion. Further increase in Eu^{3+} content up to 3 mol.% facilitates an increase in both lifetime τ_3 and intensity I_3, pointing at the continuation of the nanopore expansion process with simultaneous new pore creation. However, for $BaGa_2O_4$ ceramics with 4 mol.% Eu^{3+} ions, the opposite fragmentation process takes place, which can be described as a decreased lifetime of the third component and its increased intensity. Total nanopore volume is smaller than it is for undoped ceramics (see Table 3), thus indicating the excess character of such Eu^{3+} doping.

Thus, PAL spectroscopy can be a tool that allows us to assess the ability of Eu penetration into ceramic grains. The sites of Eu^{3+} ions define the positron trapping rate, and related structural transformations can be analyzed using positron component parameters, which change depending on the concentration of doping ions. This method can also be used to determine the size of nanopores in undoped and doped ceramic materials.

4. Conclusions

The structural features and evolution of free-volume defects in $BaGa_2O_4$ ceramics obtained by solid-phase synthesis from the initial $BaCO_3$ and Ga_2O_3 components with the addition of different amounts of Eu_2O_3 content (1, 3 and 4 mol.%) were investigated. The structural features of ceramics were studied using XRD as well as SEM with an EDX elemental analysis. It is established that, according to the quantitative analysis of the elemental composition, samples of the undoped $BaGa_2O_4$ ceramics have the largest deviations from the stoichiometric composition; they have three phases. Such processes are apparently caused by the evaporation of the constituent synthesis powders during the annealing process at high temperatures. The detected signs correlate with the XRD data.

Additional phases in ceramics are mainly localized near the grain boundaries and create defective centers for positron capture studied by PAL spectroscopy. Analyzing the second component of the PAL spectra for the undoped and Eu^{3+}-doped $BaGa_2O_4$ ceramics, it was shown that an increase in Eu^{3+} content from 1 to 3 mol.% leads to the agglomeration of free-volume defects near the grain boundaries of ceramics. At the same time, nanopores in ceramics expand and their number increases. Further increase in the content of Eu^{3+} ions is accompanied with the fragmentation of both free-volume defects and nanopores.

Results obtained by PAL spectroscopy can serve as a research base for the development of independent complementary methods for studying nanosized free volumes in ceramic materials, including neutron and heavy ion irradiated $MgAl_2O_4$ spinels [22,27,48], Si_3N_4 [49], Ge_3N_4 [50] and AlN [51–53], which are especially promising as diagnostic materials for nuclear applications. Other interesting and very important areas are the understanding of porosity, its development and transformation in electrochemical and other devices for energy conversion [54–64].

References

1.　Noto, L.L.; Poelman, D.; Orante-Barrón, V.R.; Swart, H.C.; Mathevula, L.E.; Nyenge, R.; Chithambo, M.; Mothudi, B.M.; Dhlamini, M.S. Photoluminescence and thermoluminescence properties of BaGa$_2$O$_4$. *Phys. B Condens. Matter* **2018**, *535*, 268–271. [CrossRef]

2.　Kodu, M.; Avarmaa, T.; Mändar, H.; Jaaniso, R. Pulsed Laser Deposition of BaGa$_2$O$_4$. *Appl. Phys. A* **2008**, *93*, 801–805. [CrossRef]

3.　Gust, D.; Moore, T.A.; Moore, A.L. Solar Fuels via Artificial Photosynthesis. *Acc. Chem. Res.* **2009**, *42*, 1890–1898. [CrossRef]

4.　Skillen, N.; Robertson, P.K.J. Artificial photosynthesis. In *Solar Energy*; World Scientific Publishing Co. Pte. Ltd.: Singapore, 2016; pp. 205–241. [CrossRef]

5.　Acuña, W.; Tellez, J.F.; Macías, M.A.; Roussel, P.; Ricote, S.; Gauthier, G.H. Synthesis and Characterization of BaGa$_2$O$_4$ and Ba$_3$Co$_2$O$_6$(CO$_3$)$_{0.6}$ Compounds in the Search of Alternative Materials for Proton Ceramic Fuel Cell (PCFC). *Solid State Sci.* **2017**, *71*, 61–68. [CrossRef]

6.　Guérineau, T.; Strutynski, C.; Skopak, T.; Morency, S.; Hanafi, A.; Calzavara, F.; Ledemi, Y.; Danto, S.; Cardinal, T.; Messaddeq, Y.; et al. Extended Germano-Gallate Fiber Drawing Domain: From Germanates to Gallates Optical Fibers. *Opt. Mater. Express* **2019**, *9*, 2437–2445. [CrossRef]

7.　Gonçalves, J.M.; Munoz, R.A.; Angnes, L. Materials for Optical, Magnetic and Electronic Devices. *J. Mater. Chem. C* **2021**, *9*, 8708–8717. [CrossRef]

8.　Nakauchi, D.; Okada, G.; Kawaguchi, N.; Yanagida, T. Luminescent and Scintillation Properties of Eu-Doped (Ba, Sr)Al$_2$O$_4$ Crystals. *Opt. Mater.* **2019**, *87*, 58–62. [CrossRef]

9.　Khattab, T.A.; Abd El-Aziz, M.; Abdelrahman, M.S.; El-Zawahry, M.; Kamel, S. Development of Long-persistent Photoluminescent Epoxy Resin Immobilized with Europium (II)-doped Strontium Aluminate. *Luminescence* **2020**, *35*, 478–485. [CrossRef]

10.　Yu, L.; den Engelsen, D.; Gorobez, J.; Fern, G.R.; Ireland, T.G.; Frampton, C.; Silver, J. Crystal Structure, Photoluminescence and Cathodoluminescence of Sr$_{1-x}$Ca$_x$Al$_2$O$_4$ Doped with Eu^{2+}. *Opt. Mater. Express* **2019**, *9*, 2175–2195. [CrossRef]

11.　Maphiri, V.M.; Mhlongo, M.R.; Hlatshwayo, T.T.; Motaung, T.E.; Koao, L.F.; Motloung, S.V. Citrate Sol-Gel Synthesis of BaAl$_2$O$_4$:X% Cu^{2+} (0 ≤ x ≤ 1) Nano-Phosphors: Structural, Morphological and Photoluminescence Properties. *Opt. Mater.* **2020**, *109*, 110244. [CrossRef]

12.　den Engelsen, D.; Fern, G.R.; Ireland, T.G.; Yang, F.; Silver, J. Photoluminescence and Cathodoluminescence of BaAl$_2$O$_4$:Eu^{2+} and Undoped BaAl$_2$O$_4$: Evidence for F-Centres. *Opt. Mater. Express* **2020**, *10*, 1962–1980. [CrossRef]

13.　den Engelsen, D.; Fern, G.R.; Ireland, T.G.; Silver, J. Laser-Activated Luminescence of BaAl$_2$O$_4$:Eu. *ECS J. Solid State Sci. Technol.* **2020**, *9*, 026001. [CrossRef]

14.　Shivaramu, N.J.; Coetsee, E.; Roos, W.D.; Nagabhushana, K.R.; Swart, H.C. Charge Carrier Trapping Processes in Un-Doped and BaAl$_2$O$_4$:Eu^{3+} Nanophosphor for Thermoluminescent Dosimeter Applications. *J. Phys. D Appl. Phys.* **2020**, *53*, 475305. [CrossRef]

15.　Xie, Q.; Li, B.; He, X.; Zhang, M.; Chen, Y.; Zeng, Q. Correlation of Structure, Tunable Colors, and Lifetimes of (Sr, Ca, Ba)Al$_2$O$_4$:Eu^{2+}, Dy^{3+} Phosphors. *Materials* **2017**, *10*, 1198. [CrossRef] [PubMed]

16.　Wang, S.; Wang, Y.; Gao, H.; Li, J.; Fang, L.; Yu, X.; Tang, S.; Zhao, X.; Sun, G. Synthesis and Characterization of BaAl$_2$O$_4$: Ce and Mn-Ce-Co-Doped BaAl$_2$O$_4$ Composite Materials by a Modified Polyacrylamide Gel Method and Prediction of Photocatalytic Activity Using Artificial Neural Network (ANN) Algorithm. *Optik* **2020**, *221*, 165363. [CrossRef]

17.　Malkamäki, M.; Bos, A.J.J.; Dorenbos, P.; Lastusaari, M.; Rodrigues, L.C.V.; Swart, H.C.; Hölsä, J. Persistent Luminescence Excitation Spectroscopy of BaAl$_2$O$_4$:Eu^{2+},Dy^{3+}. *Phys. B Condens. Matter* **2020**, *593*, 411947. [CrossRef]

18.　Nakauchi, D.; Okada, G.; Kato, T.; Kawaguchi, N.; Yanagida, T. Crystal Growth and Scintillation Properties of Eu:BaAl$_2$O$_4$ Crystals. *Radiat. Meas.* **2020**, *135*, 106365. [CrossRef]

19.　Vrankić, M.; Šarić, A.; Bosnar, S.; Pajić, D.; Dragović, J.; Altomare, A.; Falcicchio, A.; Popović, J.; Jurić, M.; Petravić, M.; et al. Magnetic Oxygen Stored in Quasi-1D Form within BaAl$_2$O$_4$ Lattice. *Sci. Rep.* **2019**, *9*, 15158. [CrossRef] [PubMed]

20.　Lisovskii, S.; Meganov, A.; Khrustov, V.R.; Ivanov, V. Ultraviolet Cathodoluminescence of Pure Zinc Aluminate ZnAl$_2$O$_4$. *J. Phys. Conf. Ser.* **2019**, *1410*, 012089. [CrossRef]

21.　Valiev, D.; Khasanov, O.; Dvilis, E.; Stepanov, S.; Paygin, V.; Ilela, A. Structural and Spectroscopic Characterization of Tb^{3+}-Doped MgAl$_2$O$_4$ Spinel Ceramics Fabricated by Spark Plasma Sintering Technique. *Phys. Status Solidi (B)* **2020**, *257*, 1900471. [CrossRef]

22.　Lushchik, A.; Feldbach, E.; Kotomin, E.A.; Kudryavtseva, I.; Kuzovkov, V.N.; Popov, A.I.; Seeman, V.; Shablonin, E. Distinctive Features of Diffusion-Controlled Radiation Defect Recombination in Stoichiometric Magnesium Aluminate Spinel Single Crystals and Transparent Polycrystalline Ceramics. *Sci. Rep.* **2020**, *10*, 7810. [CrossRef] [PubMed]

23.　Mironova-Ulmane, N.; Popov, A.I.; Krieke, G.; Antuzevics, A.; Skvortsova, V.; Elsts, E.; Sarakovskis, A. Low-Temperature Studies of Cr^{3+} Ions in Natural and Neutron-Irradiated g-Al Spinel. *Low Temp. Phys.* **2020**, *46*, 1154–1159. [CrossRef]

24.　Platonenko, A.; Gryaznov, D.; Kotomin, E.A.; Lushchik, A.; Seeman, V.; Popov, A.I. Hybrid Density Functional Calculations of Hyperfine Coupling Tensor for Hole-Type Defects in MgAl$_2$O$_4$. *Nucl. Instrum. Methods Phys. Res. Sect. B Beam Interact. Mater. At.* **2020**, *464*, 60–64. [CrossRef]

25.　Li, Q.; Liu, T.; Xu, X.; Wang, X.; Guo, R.; Jiao, X.; Lu, Y. Study on the Optical Spectra of MgAl$_2$O$_4$ with Oxygen Vacancies. *Mater. Technol.* **2021**, *36*, 279–285. [CrossRef]

26.　Li, Q.; Liu, T.; Xu, X.; Guo, R.; Jiao, X.; Wang, X.; Lu, Y. Study of Cation Vacancies with Localized Hole States in MgAl$_2$O$_4$ Crystals. *J. Phys. Chem. Solids* **2020**, *145*, 109542. [CrossRef]

27. Seeman, V.; Feldbach, E.; Kärner, T.; Maaroos, A.; Mironova-Ulmane, N.; Popov, A.I.; Shablonin, E.; Vasil'chenko, E.; Lushchik, A. Fast-Neutron-Induced and as-Grown Structural Defects in Magnesium Aluminate Spinel Crystals with Different Stoichiometry. *Opt. Mater.* **2019**, *91*, 42–49. [CrossRef]

28. Gholami, Y.H.; Yuan, H.; Wilks, M.Q.; Josephson, L.; el Fakhri, G.; Normandin, M.D.; Kuncic, Z. Positron Annihilation Localization by Nanoscale Magnetization. *Sci. Rep.* **2020**, *10*, 20262. [CrossRef]

29. Rementeria, R.; Domínguez-Reyes, R.; Capdevila, C.; Garcia-Mateo, C.; Caballero, F.G. Positron Annihilation Spectroscopy Study of Carbon-Vacancy Interaction in Low-Temperature Bainite. *Sci. Rep.* **2020**, *10*, 487. [CrossRef]

30. Dlubek, G.; Kilburn, D.; Bondarenko, V.; Pionteck, J.; Krause-Rehberg, R.; Alam, M.A. Positron Annihilation: A Unique Method for Studying Polymers. *Macromol. Symp.* **2004**, *210*, 11–20. [CrossRef]

31. Dai, H.Y.; Liu, H.Z.; Peng, K.; Ye, F.J.; Li, T.; Chen, J.; Chen, Z.P. Correlation between Vacancy Defects and Magnetic Properties of the $GdMn_{1-x}Zn_xO_3$ Multiferroic Ceramics Studied by Positron Annihilation. *Mater. Res. Bull.* **2019**, *119*, 110565. [CrossRef]

32. Barad, D.; Mange, P.L.; Jani, K.K.; Mukherjee, S.; Ahmed, M.; Kumar, S.; Dolia, S.N.; Pandit, R.; Raval, P.Y.; Modi, K.B.; et al. Ca^{2+}-Substitution Effect on the Defect Structural Changes in the Quadruple Perovskite Series $Ca_{1+x}Cu_{3-x}Ti_4O_{12}$ Studied by Positron Annihilation and Complementary Methods. *Ceram. Int.* **2021**, *47*, 2631–2640. [CrossRef]

33. Ghanem, A.; Mohamed, K. Effect of Gamma-Ray on Producing Induced Colour Centres and on Positron Annihilation Lifetime of Bismuth-Doped Zinc Sodium Borate Glasses. *Arab. J. Nucl. Sci. Appl.* **2021**, *54*, 1–9. [CrossRef]

34. Ashok, J.; Kostrzewa, M.; Ingram, A.; Reddy, M.S.; Kumar, V.R.; Gandhi, Y.; Veeraiah, N. Free Volume Estimation in Au and Ag Mixed Sodium Antimonate Glass Ceramics by Means of Positron Annihilation. *Phys. B Condens. Matter* **2019**, *570*, 266–273. [CrossRef]

35. El-Gamal, S.; Elsayed, M. Positron Annihilation and Electrical Studies on the Influence of Loading Magnesia Nanoribbons on PVA-PVP Blend. *Polym. Test.* **2020**, *89*, 106681. [CrossRef]

36. Zhang, H.J.; Sellaiyan, S.; Sako, K.; Uedono, A.; Taniguchi, Y.; Hayashi, K. Effect of Free-Volume Holes on Static Mechanical Properties of Epoxy Resins Studied by Positron Annihilation and PVT Experiments. *Polymer* **2020**, *190*, 122225. [CrossRef]

37. Biswas, D.; Rajan, A.; Kabi, S.; Das, A.S.; Singh, L.S.; Nambissan, P.M.G. Structural Defects Characterization of Silver-Phosphate Glass Nanocomposites by Positron Annihilation and Related Experimental Studies. *Mater. Charact.* **2019**, *158*, 109928. [CrossRef]

38. Fan, J.; Zhou, W.; Wang, Q.; Chu, Z.; Yang, L.; Yang, L.; Sun, J.; Zhao, L.; Xu, J.; Liang, Y.; et al. Structure Dependence of Water Vapor Permeation in Polymer Nanocomposite Membranes Investigated by Positron Annihilation Lifetime Spectroscopy. *J. Membr. Sci.* **2018**, *549*, 581–587. [CrossRef]

39. Sato, K.; Tamiya, R.; Xu, Q.; Tsuchida, H.; Yoshiie, T. Detection of Deuterium Trapping Sites in Tungsten by Thermal Desorption Spectroscopy and Positron Annihilation Spectroscopy. *Nucl. Mater. Energy* **2016**, *9*, 554–559. [CrossRef]

40. Wang, Z.F.; Wang, B.; Yang, Y.R.; Hu, C.P. Correlations between Gas Permeation and Free-Volume Hole Properties of Polyurethane Membranes. *Eur. Polym. J.* **2003**, *39*, 2345–2349. [CrossRef]

41. Melikhova, O.; Kuriplach, J.; Prochazka, I.; Cizek, J.; Hou, M.; Zhurkin, E.; Pisov, S. Simulation of Positron Annihilation Response to Mechanical Deformation of Nanostructured Ni_3Al. *Appl. Surf. Sci.* **2008**, *255*, 157–159. [CrossRef]

42. Shpotyuk, O.; Balitska, V.; Brunner, M.; Hadzaman, I.; Klym, H. Thermally-Induced Electronic Relaxation in Structurally-Modified $Cu_{0.1}Ni_{0.8}Co_{0.2}Mn_{1.9}O_4$ Spinel Ceramics. *Phys. B Condens. Matter* **2015**, *459*, 116–121. [CrossRef]

43. Klym, H.; Ingram, A.; Shpotyuk, O.; Karbovnyk, I. Influence of CsCl Addition on the Nanostructured Voids and Optical Properties of $80GeS_2$-$20Ga_2S_3$ Glasses. *Opt. Mater.* **2016**, *59*, 39–42. [CrossRef]

44. Kostiv, Y.; Luchechko, A.; Klym, H.; Karbovnyk, I.; Sadovyi, B.; Zaremba, O.; Kravets, O. Structural properties of polycrystalline $BaGa_2O_4$ Ceramics Doped with Eu^{3+} Ions. In Proceedings of the XIth International Scientific and Practical Conference on Electronics and Information Technologies, Lviv, Ukraine, 16–18 September 2019; pp. 307–311. [CrossRef]

45. Klym, H.; Ingram, A.; Hadzaman, I.; Shpotyuk, O. Evolution of Porous Structure and Free-volume Entities in Magnesium Aluminate Spinel Ceramics. *Ceram. Int.* **2014**, *40*, 8561–8567. [CrossRef]

46. Kansy, J.; Giebel, D. Study of Defect Structure with New Software for Numerical Analysis of PAL Spectra. *J. Phys. Conf. Ser.* **2011**, *265*, 0102030. [CrossRef]

47. Goworek, T. Comments on the Relation: Positronium Lifetime—Free Volume Size Parameters of the Tao-Eldrup Model. *Chem. Phys. Lett.* **2002**, *366*, 184–187. [CrossRef]

48. Lushchik, A.; Dolgov, S.; Feldbach, E.; Pareja, R.; Popov, A.I.; Shablonin, E.; Seeman, V. Creation and Thermal Annealing of Structural Defects in Neutron-Irradiated $MgAl_2O_4$ Single Crystals. *Nucl. Instrum. Methods Phys. Res. Sect. B Beam Interact. Mater. At.* **2018**, *435*, 31–37. [CrossRef]

49. Feldbach, E.; Museur, L.; Krasnenko, V.; Zerr, A.; Kitaura, M.; Kanaev, A. Defects Induced by He^+ Irradiation in γ-Si_3N_4. *J. Lumin.* **2021**, *237*, 118132. [CrossRef]

50. Feldbach, E.; Zerr, A.; Museur, L.; Kitaura, M.; Manthilake, G.; Tessier, F.; Krasnenko, V.; Kanaev, A. Electronic Band Transitions in γ-Ge_3N_4. *Electron. Mater. Lett.* **2021**, *17*, 315–323. [CrossRef]

51. Kozlovskiy, A.; Kenzhina, I.; Zdorovets, M.V. Optical and Structural Properties of AlN Ceramics Irradiated with Heavy Ions. *Opt. Mater.* **2019**, *91*, 130–137. [CrossRef]

52. Zdorovets, M.V.; Dukenbayev, K.; Kozlovskiy, A.L. Study of Helium Swelling in Nitride Ceramics at Different Irradiation Temperatures. *Materials* **2019**, *12*, 2415. [CrossRef] [PubMed]

53. Kozlovskiy, A.; Kenzhina, I.; Dukenbayev, K.; Zdorovets, M. Influence of He-ion Irradiation of Ceramic AlN. *Vacuum* **2019**, *163*, 45–51. [CrossRef]

54. Kurteeva, A.A.; Bogdanovich, N.M.; Bronin, D.I.; Porotnikova, N.M.; Vdovin, G.K.; Pankratov, A.A.; Beresnev, S.M.; Kuz'mina, L.A. Options for Adjustment of Microstructure and Conductivity of Cathodic Substrates of La(Sr)MnO$_3$. *Russ. J. Electrochem.* **2010**, *46*, 811–819. [CrossRef]

55. Porotnikova, N.M.; Eremin, V.A.; Farlenkov, A.S.; Kurumchin, E.K.; Sherstobitova, E.A.; Kochubey, D.I.; Ananyev, M.V. Effect of AO Segregation on Catalytical Activity of La$_{0.7}$A$_{0.3}$MnO$_{3\pm\delta}$ (A = Ca, Sr, Ba) Regarding Oxygen Reduction Reaction. *Catal. Lett.* **2018**, *148*, 2839–2847. [CrossRef]

56. Osinkin, D.A.; Khodimchuk, A.V.; Porotnikova, N.M.; Bogdanovich, N.M.; Fetisov, A.V.; Ananyev, M.V. Rate-Determining Steps of Oxygen Surface Exchange Kinetics on Sr$_2$Fe$_{1.5}$Mo$_{0.5}$O$_{6-\delta}$. *Energies* **2020**, *13*, 250. [CrossRef]

57. Suchikova, Y.O. Sulfide Passivation of Indium Phosphide Porous Surfaces. *J. Nano-Electron. Phys.* **2017**, *9*, 01006. [CrossRef]

58. Suchikova, J.A. Synthesis of Indium Nitride Epitaxial Layers on a Substrate of Porous Indium Phosphide. *J. Nano-Electron. Phys.* **2015**, *7*, 03017.

59. Shlimas, D.; Kenzhina, I.; Zdorovets, M. Study of the Use of Ionizing Radiation to Improve the Efficiency of Performance of Nickel Nanostructures as Anodes of Lithium-ion Batteries. *Mater. Res. Express* **2019**, *6*, 055026. [CrossRef]

60. Rumiantseva, Y.; Melnichuk, I.; Garashchenko, V.; Zaporozhets, O.; Turkevich, V.; Bushlya, V. Influence of cBN Content, Al$_2$O$_3$ and Si$_3$N$_4$ Additives and Their Morphology on Microstructure, Properties, and Wear of PCBN with NbN Binder. *Ceram. Int.* **2020**, *46*, 22230–22238. [CrossRef]

61. Olenych, I.B.; Aksimentyeva, O.I.; Monastyrskii, L.S.; Horbenko, Y.Y.; Partyka, M.V. Electrical and Photoelectrical Properties of Reduced Graphene Oxide—Porous Silicon Nanostructures. *Nanoscale Res. Lett.* **2017**, *12*, 272. [CrossRef]

62. Luchechko, A.; Zhydachevskyy, Y.; Ubizskii, S.; Kravets, O.; Popov, A.I.; Rogulis, U.; Elsts, E.; Bulur, E.; Suchocki, A. Afterglow, TL and OSL Properties of Mn^{2+}-doped ZnGa$_2$O$_4$ Phosphor. *Sci. Rep.* **2019**, *9*, 9544. [CrossRef]

63. Dimza, V.; Popov, A.I.; Lāce, L.; Kundzins, M.; Kundzins, K.; Antonova, M.; Livins, M. Effects of Mn Doping on Dielectric Properties of Ferroelectric Relaxor PLZT Ceramics. *Curr. Appl. Phys.* **2017**, *17*, 169–173. [CrossRef]

64. Bystrova, A.; Dekhtyar, Y.D.; Popov, A.; Coutinho, J.; Bystrov, V. Modified Hydroxyapatite Structure and Properties: Modeling and Synchrotron Data Analysis of Modified Hydroxyapatite Structure. *Ferroelectrics* **2015**, *475*, 135–147. [CrossRef]